INSTITUTE OF PHYSICS PUBLISHING PHYSICS IN MEDICINE AND BIOLOGY

Phys. Med. Biol. **50** (2005) 2543–2557 doi:10.1088/0031-9155/50/11/007

The Twente Photoacoustic Mammoscope: system overview and performance

Srirang Manohar[1], **Alexei Kharine**[1], **Johan C G van Hespen, Wiendelt Steenbergen and Ton G van Leeuwen**

Biophysical Engineering Group, Faculty of Science and Technology, University of Twente, PO Box 217, 7500AE Enschede, The Netherlands

E-mail: S.Manohar@tnw.utwente.nl

Received 1 November 2004
Published 18 May 2005
Online at stacks.iop.org/PMB/50/2543

Abstract

We present PAM, the Photoacoustic Mammoscope developed at the University of Twente, intended for initial retrospective clinical studies on subjects with breast tumours. A parallel plate geometry has been adopted and the breast will be gently compressed between a glass plate and a flat ultrasound detector matrix. Pulsed light (5 ns) from an Nd:YAG laser will impinge the breast through the glass plate in regions of interest; an appropriate number of the 590 elements of the detector matrix will be activated in succession to record photoacoustic signals. Three-dimensional image reconstruction employs a delay-and-sum beamforming algorithm. We discuss various instrumental aspects and the proposed imaging protocol. Performance studies of the ultrasound detector are presented in terms of sensitivity, frequency response and resolution. Details of the patient–instrument interface are provided. Finally some imaging results on well-characterized breast tissue phantoms with embedded tumour simulating inserts are shown.

(Some figures in this article are in colour only in the electronic version)

1. Introduction

The leading position of breast cancer incidence (American Cancer Society 2004) and the drawbacks of conventional mammography techniques are the motivation behind the search for newer modalities for breast cancer detection. Among the alternative techniques being developed in the last few decades (Nass *et al* 2001) optical imaging using near-infrared light (NIR) has attracted considerable interest among researchers (Pogue *et al* 2001, Grosenick *et al* 2003, Heffer and Fantini 2002). Optical imaging is popular because the

[1] These authors contributed equally to the work.

technique is relatively inexpensive, and the non-ionizing nature of NIR light makes it risk-free. Detection and localization are possible due to the presence of optical absorption contrast between tumours and healthy tissue (Tromberg *et al* 2000, Suzuki *et al* 1996, Pogue *et al* 2001). This is due to increased haemoglobin concentration as a result of angiogenesis (Folkman 2000). The haemoglobin oxygen saturation of suspicious sites can additionally serve as a criterion for diagnosing malignancy and can be reconstructed by spectroscopic analysis (Van Veen *et al* 2005, Tromberg *et al* 2000, Pogue *et al* 2001).

However, light propagating in biological tissue is highly scattered which often results in difficulties in detection and precise localization of small tumours. Improving spatial resolution and discriminating between absorption and scattering remain the biggest challenges that are faced by optical imaging.

A technique that probes the optical absorption contrast exhibited by tumours to NIR light, without having the problem associated with scattering, is photoacoustic (PA) imaging. Optical contrast on the one hand, and low scattering of ultrasound in breast tissue on the other, are brought together in this hybrid technique. Ultrasound is generated internally by absorbing sites illuminated with short pulses of laser light (Hoelen *et al* 1998). Since the technique does not 'look' for photons and the resulting ultrasound propagates with low scattering through tissue, photoacoustics yields higher resolution than purely optical techniques.

The mechanism of PA signal generation consists of the following steps: (1) light is selectively absorbed in higher absorbing regions when the investigated volume is exposed to pulsed laser radiation; (2) fast non-radiative relaxation of excited states takes place with thermalization of absorbed optical energy; (3) the resulting local thermal expansion produces pressure transients. The pressure pulses propagate as ultrasound to the surface where it is detected using wide-frequency band detectors (Hoelen *et al* 2001, Andreev *et al* 2003). The time-of-flight, amplitude and duration of the pressure transient generated under irradiation conditions of pressure and thermal confinement[2] provide information regarding location, strength and dimension of the acoustic source, thereby permitting a reconstruction of the absorber.

Two instruments for breast imaging using the photoacoustic effect[3] have been reported earlier. The thermoacoustic computed tomography (TCT) scanner uses radiation at a frequency of 434 MHz for excitation. It consists of three planar arrays with 128 elements each arranged such that when rotated around the pendant breast, provide a nearly complete coverage of the breast (Kruger *et al* 2000). The instrument maps the concentration of ionic water (not haemoglobin) in three dimensions (3D) in the breast, which is expected to be enhanced at a tumour site due to angiogenesis. Another system, the laser optoacoustic imaging system (LOIS), uses NIR light pulses at 1064 nm for excitation and an arc shaped 32 element ultrawide frequency band detection array (Oraevsky and Karabutov 2003). This system is capable of providing two-dimensional (2D) slice images of the breast. A limited number of patient measurements have been reported using both instruments (Kruger *et al* 2001, Oraevsky *et al* 1999). There have been as yet no large clinical trials and the technique is as yet at its incipient stages.

In this paper, we present a new version of a mammography system developed in the University of Twente, based on the photoacoustic principle, also using NIR light at 1064 nm. The Twente Photoacoustic Mammoscope (PAM) uses a flat ultrasound detector matrix in a parallel plate configuration. The design of the instrument is based on our experience with a laboratory prototype reported recently (Manohar *et al* 2004). We discuss various instrumental

[2] Pressure and temperature relaxation during time scale of the laser (heating) pulse duration is negligible.

[3] In this paper we refer to thermoelastic photo-generation of ultrasound as photoacoustics, whether the photons lie in the microwave, radiowave or optical range of the electromagnetic spectrum.

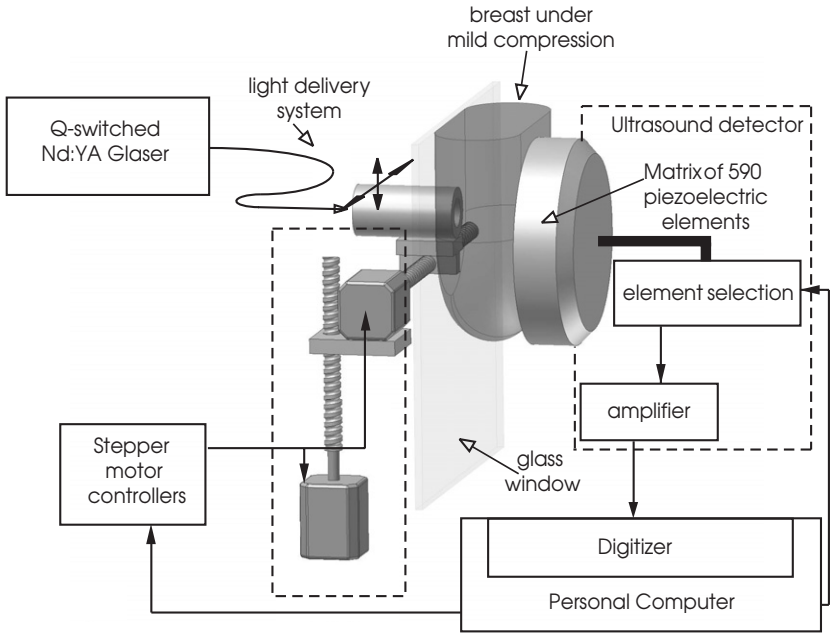

Figure 1. Schematic of the Photoacoustic Mammoscope.

aspects, details of the patient–instrument interface, and present performance studies on liquid and solid phantoms.

2. The Photoacoustic Mammoscope

A schematic of the Photoacoustic Mammoscope (PAM) is presented in figure 1. The breast is mildly compressed between a glass window and a flat detector matrix. The light source is a Q-switched Nd:YAG laser (Brilliant-B, Quantel, Paris) with a pulse duration of 5 ns and a repetition rate of 10 Hz. The pulse width of the laser is chosen to fulfil the conditions of temperature and stress confinement. The choice of laser wavelength is dictated by the fact that mammography involves imaging through large volumes of tissue; light penetration depth in breast tissue is expected to be maximum in the 1000–1100 nm region (Tromberg *et al* 2000). The light beam is coupled into a light delivery system. A scanning system translates the output of the light delivery system (LDS) in two dimensions, to locally illuminate the surface of the breast through the glass window. PA generated ultrasound propagates through the breast to be recorded by the ultrasound detector matrix at the opposite side. A number of detectors appropriate to the desired scanning area are read out. The control lines of the device are controlled via a digital input–output card in the PC. The data line is fed to 1 channel of a dual channel 100 MHz, 100 MS s^{-1}, 8 bit digitizer (NI-5112, National Instruments, Austin) card in the PC. The PC runs a LABView program that controls the scanning system, the detector array and digitizer. Three-dimensional images are reconstructed using a delay-and-sum beamforming algorithm (Hoelen *et al* 2000).

The main building blocks of the mammoscope are the ultrasound detector, the light delivery system and the patient–instrument interface.

2.1. The ultrasound detector

The heart of PAM is a large-area two-dimensional ultrasound detector array. This was developed by Lunar Corporation, General Electric (Wisconsin, Madison) for use as a receiver in an ultrasonic bone densitometer, the Achilles InSight^{TM}. We have adapted this receiver for use in photoacoustics.

The detector uses polyvinylidene fluoride (PVDF) for piezoelectric transduction. The PVDF sheet is 110 μm thick and approximately 90 mm in diameter. Thin gold electrodes have been deposited on the front and rear faces of the PVDF sheet by vacuum metallization. These electrodes numbering 590 are 2 $\times$ 2 mm square and arranged in a roughly circular grid with a centre–centre spacing of 3.175 mm. The PVDF film has been polarized by the application of an external electrical field to the electrodes. This imparts piezoelectric activity only to regions sandwiched by the electrodes and thus defines 590 active elements. The spatially selective polarization has the effect of reducing acoustic crosstalk between elements.

The film is supported at one face by an 18.6 mm thick layer of a proprietary material. This also serves as a protective layer, and is chosen with acoustic properties matching tissue. The electrical contacts to the inner face electrodes are obtained by spring-loading conductive pins against the film. The conductive pins are mounted as a 590 element grid on a printed circuit board (PCB), and lead on to signal processing and multiplexing electronics. Control line inputs to the multiplexer on the PCB allow one element to be activated at a time. The protective layer forms the front face of the device, and the entire unit with its electronics is enclosed in a chassis.

2.1.1. Element sensitivity. The sensitivity of an arbitrary element was measured by a substitution method using a calibrated hydrophone system. The hydrophone system from Precision Acoustics Ltd (Dorchester) comprised a 0.2 mm needle hydrophone (HPM 02/1), a submersible integrated preamplifier (HP1) and a dc coupler (DC2). The ultrasound (US) source was a videoscan immersion transducer (Panametrics, Waltham) with a centre frequency of 1 MHz and a focal length of 20 mm.

The detector matrix was sealed through an aperture at the bottom of a Perspex imaging tank so that the surface of the detector unit was flush with the floor of the tank, as shown in figure 2(a). The tank was filled with degassed, deionized water. The ultrasound (US) transducer was mounted on the *XY* scanning stage to be 1.5 mm from the surface of the detector, and positioned at the centre of the detector. By this the focus of the transducer lies in the element plane. The transducer was excited with a one cycle burst of a 1 MHz sine wave, with a peak–peak voltage of 0.5 V, and repetition rate 1 kHz, using a function generator (Model 33250A, Agilent Technologies, Palo Alto).

Positioning of the US source to focus onto an element, hidden by the opaque protective layer, was performed as follows. The central element was activated and signals received were monitored using the digitizer. The transducer was then scanned in steps of 0.5 mm around its initial position till the acquired signal intensity obtained as the peak–peak voltage was strongest, indicating that the element was in the focus of the transducer.

Under this condition the excitation to the transducer was reduced from a high value to the point where the signal-to-noise ratio (SNR) of the received ultrasound pulse reduced to 1. Signals were acquired by averaging 128 times.

These procedures were repeated, substituting the ultrasound detector array with the hydrophone system. With a knowledge of the sensitivity of the hydrophone system from the calibration curve as 36.9 mV MPa^{-1} (uncertainty 14%) at 1 MHz, an approximate source transfer function was obtained in pressure units versus excitation input. From this the

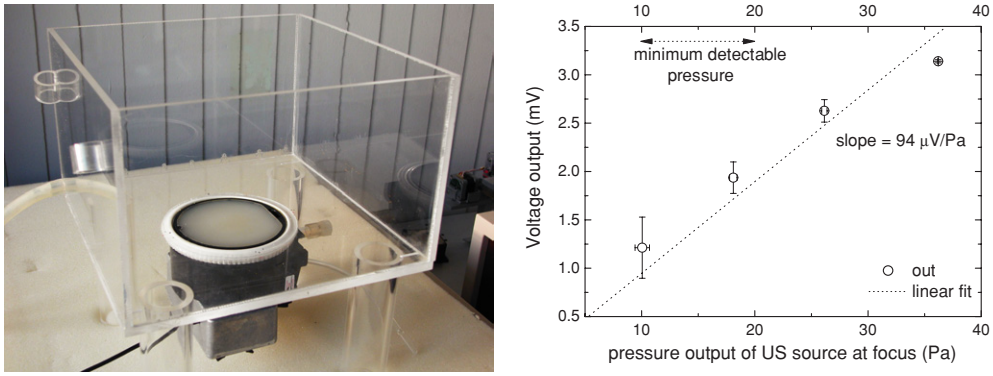

(a) (b)

Figure 2. (a) For characterization and phantom experiments, the ultrasound detector matrix is mounted through an aperture in the imaging tank, so that its surface is flush with the floor of the tank. (b) Sensitivity curve and minimum detectable pressure of the central element of the detector array, obtained using an ultrasound source of known transfer function. Signals were acquired after 128 averages.

end-of-cable sensitivity (including signal processing electronics) of the detection element was estimated from the voltage output versus the pressure incident on the element, as shown in figure 2(b). An end-of-cable sensitivity of 95 μV Pa^{-1} and an approximate minimum detectable pressure of 10 Pa at 1 MHz with 128 averages may be ascertained from the graph. The noise equivalent pressure obtained from single-sampled measurements is a factor of 10 higher and is about 100 Pa.

It must be mentioned that this method is approximate since the US source possesses a finite bandwidth, and the calibration curve of the hydrophone system is specified at discrete frequencies. A more accurate measurement of sensitivity is possible using a nonlinear wave propagation substitution procedure (Smith and Bacon 1990) and this is the subject of ongoing investigation.

2.1.2. Inter-element performance. In order to ascertain the element–element variations in sensitivity, a tandem method of measurement was undertaken. In this, after the position of the US source above the central element of the matrix was established as in section 2.1.1, the source was mechanically scanned in the x and y directions in steps of 3.175 mm (the inter-element spacing). At each position of the source, the appropriate element (if present) was activated and the signal recorded. The distance of the source from the element plane was maintained around 10 mm greater than the focal length. This was to reduce the effect of small errors in laterally positioning the source above the elements.

The peak–peak value of the recorded signals where the US pulse is expected is plotted as a C-scan image in figure 3(a), to obtain a map of element positions. The roughly circular arrangement of the elements is clearly seen where finite peak–peak signals were recorded. Variations between six rows of the matrix are shown in figure 3(b). It is seen that the central section of the detector shows uniform outputs. The low outputs of the edge elements are probably due to their close proximity to the detector wall; it is likely that the elements are not well insonified by the source output due to its interaction with the wall surface.

2.1.3. Frequency response. Ultrasound pulses generated photoacoustically from spherical absorbers are bipolar with a positive (compressive) peak and a negative (rarefaction) peak.

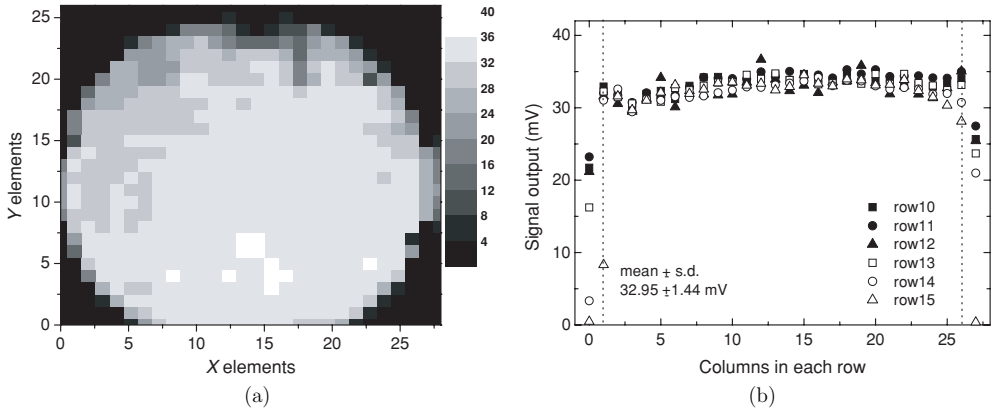

Figure 3. (a) Inter-element performance obtained by scanning an ultrasound source above the detector in steps equal to element pitch. A circular arrangement of elements is clearly seen. It is likely that the wall of the detector interferes with the beam of the ultrasound source along the edges; the edge elements show lower outputs. Some defective elements can also be identified. (b) Values of the peak–peak voltages from a selection of rows in the matrix. The mean has been calculated by masking the edge element outputs.

The duration of the pulse is related to the size of the absorber, with the peak–peak time (Sigrist and Kneubühl 1978):

$$\tau_{pp} = \sqrt{2}\frac{r_0}{v}, \tag{1}$$

where r_0 is the radius of the absorber, and v the acoustic velocity.

The Fourier spectrum of a bipolar PA pulse reveals that the major portion of the acoustic energy is concentrated in a bandwidth (Oraevsky *et al* 2001, Andreev *et al* 2003) given by:

$$f_b = 0.75\frac{v}{r_0}. \tag{2}$$

Thus, it is obvious then that the ability of an ultrasound detector to faithfully represent PA transients of absorbers over a range of sizes is determined by the frequency bandwidth of its elements.

Measurements of the frequency response of an element were performed using an impulsive wave method. When the optical penetration depth (δ) in an absorber is smaller than the laser pulse duration dictated resolution, the PA transient produced can be likened to an impulse. The condition is represented as:

$$\delta = \frac{1}{\mu_a} < \tau_l v, \tag{3}$$

where μ_a is the absorption coefficient, and τ_l the laser pulse duration.

India Ink (Royal Talens, Apeldoorn), characterized for its absorption coefficient using a spectrophotometer (Shimadzu UV-3101 PC, Tokyo), was used as the absorber. A dilution of 50% India ink in water (μ_a of 214 mm^{-1} at 1064 nm) was used. A Perspex plate of 5 mm thickness was used to sandwich 30 mm of the ink solution against the detector surface. A Q-switched Nd:YAG laser with a pulse width of 9 ns (Quanta Ray PDL-2, Spectra Physics, California) and a beam diameter of 8 mm was used for illumination. Signals were recorded from an element directly beneath the impinging laser beam. Under these experimental conditions the signal represents the end-of-cable impulse response of the element including the characteristics of the electronics. Figure 4(a) is a typical signal trace for a fluence

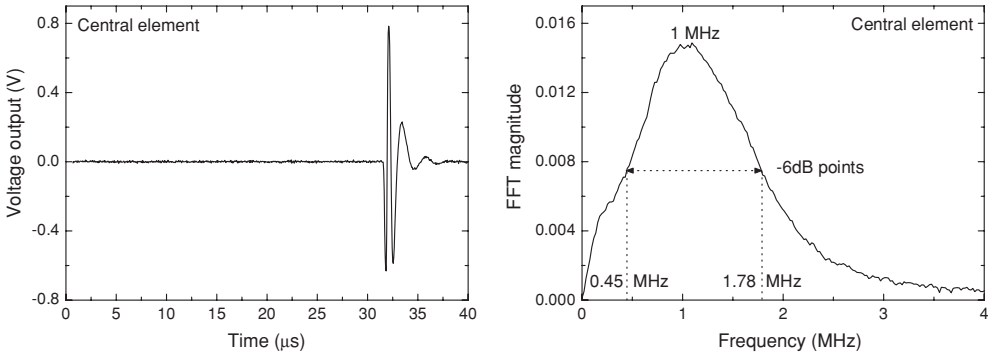

Figure 4. (a) Signal trace recorded from the central element of the detector matrix following photoacoustic generation in India Ink solution. The experimental conditions ensure that this is the end-of-cable impulse response of the detector element. (b) Frequency response of the detector element obtained by Fourier transforming the photoacoustic transient. The −6 dB fractional frequency bandwidth is 130%.

rate of 25 mJ cm^{-2} at the surface. Figure 4(b) is the Fourier transform of the transient, which shows the broadband nature of the system, with the −6 dB bandwidth extending from 450 kHz to 1.78 MHz. The maximum frequency detectable with the system is around 2.5 MHz.

The maximum frequency can be used to estimate the minimum radius of a sphere that can be faithfully registered by an element. A guideline for this estimation (Andreev *et al* 2003) is based on:

$$r_{o_{min}} = 1.5\frac{v}{f_{max}}, \tag{4}$$

which yields a diameter of 1.8 mm as the smallest sphere that can be resolved by an element.

2.1.4. Resolution. The spatial resolution of an ultrasound detector array is known to depend upon the number of detector elements, inter-element spacing, directional sensitivity of the elements, distance between detector and ultrasound source, and frequency response of the elements (Oraevsky *et al* 2001, Xu and Wang 2003, Andreev *et al* 2003). In addition, the resolution of the system also depends on the image reconstruction algorithm that is employed.

The single-point definition of resolution sets the resolution as the FWHM (full width at half maximum) of the point-spread function (PSF). A two-point definition is the Rayleigh criterion which defines resolution as that distance between two points at which the peak of the PSF of one occurs where the PSF of the second first falls to zero.

We undertook measurements based on both these criteria. Dyed poly(vinyl alcohol) gel spheres without scattering and with an absorption coefficient (μ_a) of 0.25 mm^{-1} (Kharine *et al* 2003, Manohar *et al* 2004) were fashioned with a scalpel to obtain approximately 2 mm diameter spheres. One or two spheres, depending on whether a single- or two-PSF experiment was being performed, were suspended using a nylon thread (80 μm diameter) in the imaging tank. The spheres were positioned approximately in the centre of the detector matrix. The tank was filled with 4% Intralipid 10% stock solution (Fresenius Kabi, Bad Homburg) so that the spheres were 10 mm below the surface. This solution possesses a low scattering coefficient of 0.3 mm^{-1} at 1064 nm (Van Staveren *et al* 1991).

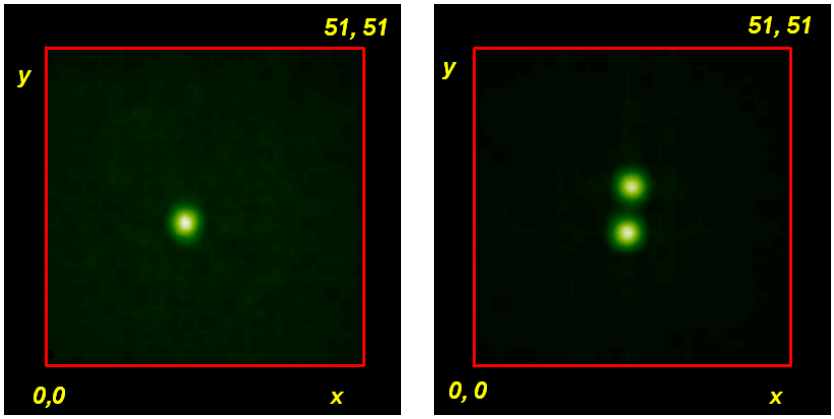

(a) (b)

Figure 5. Top view maximum intensity projections (MIPs) of reconstructed data from (a) a single 2 mm diameter absorbing sphere, and (b) two 2 mm diameter absorbing spheres with a separation of 5.5 mm, in low scattering Intralipid. The detector–sphere(s) distance in both cases was 30 mm.

Light from the Nd:YAG laser was allowed to fall on the spheres, and the elements in a square area of 52 × 52 mm area of the detector were activated in succession. This area corresponds to the scanning area that will be used for the first clinical trials of the instrument. The signal traces from each element acquired by the digitizer were saved in the PC to form the inputs to the image reconstruction program based on the delay-and-sum beamforming algorithm. (See section 3 further.) The strong PA signals generated from the surface were excluded in the reconstructions. The voxel sizes chosen were 0.5 × 0.5 × 0.5 mm; the window size was chosen as 2 mm. The data set was normalized to the highest intensity in the data matrix and scaled to 256.

Figures 5(a) and (b) show representative top-view maximum intensity projections (MIPs) of single- and two-PSFs for a detector–spheres distance of 30 mm. Gaussians were fitted to the PSFs in both x and y directions through the centres of the spheres in XY slices through the sphere centres. Figures 6(a) and (b) show the fitted data along y directions for the slices. From the single-PSF analysis, the lateral resolution could be ascertained as twice the standard deviation of the PSF's Gaussian fit. Axial resolution was estimated in a similar manner by considering the appropriate slices through the single-PSFs in XZ and YZ planes, with fitting along the z direction.

The analysis of the single-PSF measurements yields equivalent results to two-PSF experiments. It was then decided to pursue single-PSF experiments to ascertain the spatial resolution, since two-PSF experiments are inconvenient and error prone especially since resolution has to be defined at different distances from the detector.

From analyses of single-PSF experiments at different distances of the sphere from the detector it could be concluded that the lateral resolution of the system (including the image reconstruction algorithm) ranged from 3.1 mm (at 15 mm distance from the detector) to 4.4 mm (at 60 mm distance); the axial resolution from 3.2 mm (15 mm distance) to 3.9 mm (60 mm distance).

2.2. Light delivery system (LDS)

The choice of an appropriate mechanism to deliver light to the breast surface was guided by a combination of two factors: the maximum permissible exposure to light on human tissue,

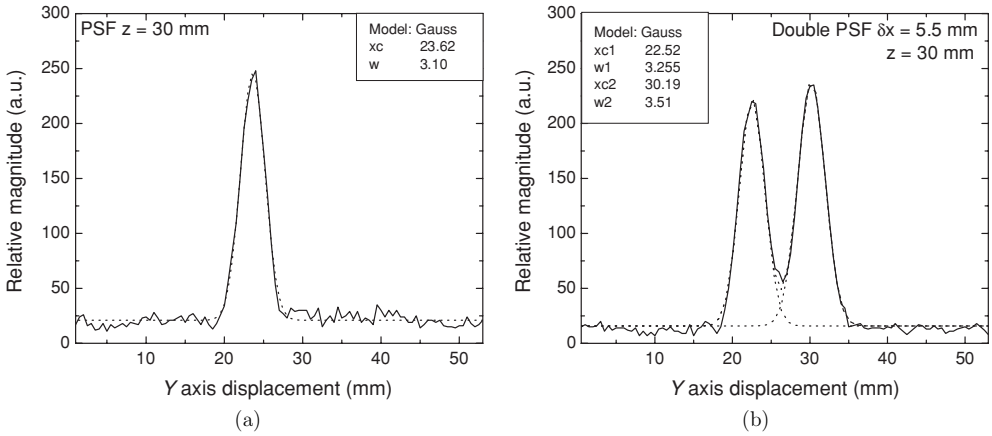

Figure 6. Profiles through the point-spread functions (PSFs) for *XY* slices through the sphere centres. The data have been fitted to Gaussian distributions. The relevant parameters of the fit are shown in the inset; 'xc' the mean, estimates the centre of the PSF; 'w' twice the standard deviation estimates the width of the PSF.

and the energy required to perform deep (30+ mm) imaging in phantoms. The MPE for the class of laser used is specified as 20 mJ cm^{-2} per pulse. It was also found that at least 50 mJ of light distributed over 2.5 cm^2 at 1064 nm was required to perform deep imaging. Thus it was decided to look for a mechanism that would permit energies of this order and higher to be transported; and with additional facility for beam expansion at the output.

The use of various delivery systems was investigated for this application: single silica fibres, silica fibre bundles and liquid light guides. All of these were ultimately rejected owing to their inability in reliably transporting the energies required without damage.

A commercially available articulated arm with multiple articulating joints and mirrors was briefly considered but rejected owing to superfluity of degrees of freedom for the planar measurement and scanning geometry adopted in PAM. It was then decided to develop a custom-designed system based on reflecting prisms specific to the mammoscope. This light delivery system (LDS) is shown in figure 7(a). It comprises two movable joints and two prisms.

Prisms were favoured over coated mirrors due to their higher power handling capability. Prism 1 (at bottom in figure 7(a)) is mounted on a carriage which slides along a guiding rail as shown. Light enters along rotation axis 1, through a hollow flanged tube, the free end of which is anchored to the laser. The tube is fixed as shaft of rotary bearing 1, mounted in a housing on carriage 1 (see figure 7(a)).

The output of prism 2 (top in figure) is through a similar hollow tube whose free end is anchored to the payload of an *XY* scanning system. See also figure 8. The rail is chosen to be longer than the farthest excursion possible with the prism 2 carriage as payload in the scanning system. The rail is floating and not fixed to any structure. It allows the prism 2 holder to be translated in the x and y directions, and along with the rotary bearings helps the prisms maintain the same relative orientation ensuring parallelism between the input and output beams.

It is also possible to illuminate one or the other surface of the compressed breast as shown in figure 7(b). This is made possible by the mounting of prism 2 on rotary bearing 2, which provides additional rotation in a plane perpendicular to the *XY* plane. See further in section 2.3.

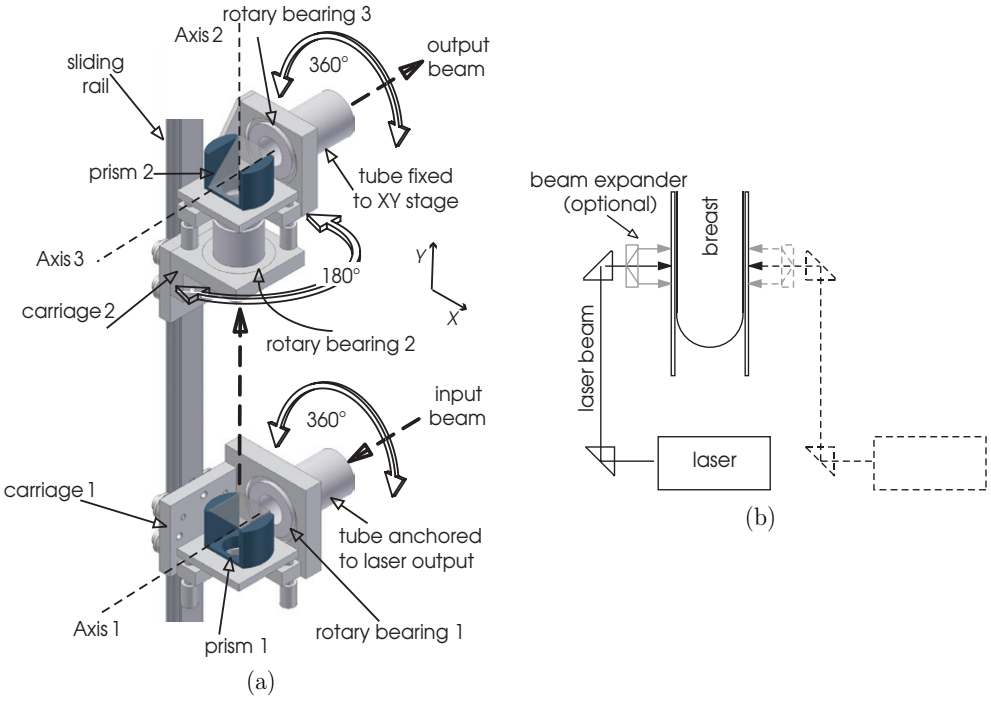

Figure 7. The custom-designed light delivery system: (a) mechanical construction; the input is fitted to the laser, the output mounted on an *XY* scanning system, (b) possible modes of illumination of breast.

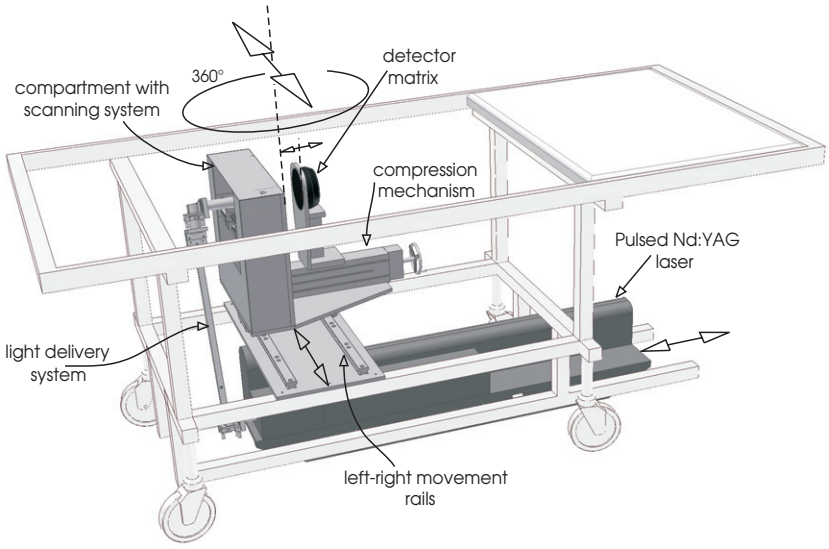

Figure 8. The Photoacoustic Mammoscope. The instrument is built into a hospital bed. The top plates of the bed are not shown.

2.3. Patient–instrument interface

The instrument is built into a hospital bed as shown in figure 8. The subject lies prone on the bed with her breast pendant through the aperture (not shown) in the bed. The breast is mildly compressed between the detector matrix and the glass plate of a compartment which carries an *XY* scanning system. Compression is required to obtain a uniform thickness of the breast and a good acoustic contact with the detector. This is achieved by manually turning the handwheel of the compression mechanism. The scanning system based on lead screws has as payload the output of the light delivery assembly. The base of the instrument is mounted on carriages which run on the rails; depending on whether the symptomatic breast is the left one or right; the instrument can be slid accordingly.

The standard examination will comprise a craniocaudal (CC) examination, with illumination on the top surface of the breast, and detection at the bottom. Laboratory phantom studies have revealed that imaging depth may be restricted to 30–35 mm, in which case for thicker breasts a second caudocranial (CC-FB from below) may be required, with the illumination-detection sides exchanged. The instrument base is mounted on an angular bearing which allows the base to be rotated on its axis. After a CC scan, the breast is retracted, the LDS detached at the scanning system end. The instrument is then rotated through 180°; the laser is slid backward (a linear guidance system is provided for this). The LDS output is then rotated through 180° along axis 2 (see figure 7(a)) and then reattached to the scanning system to permit a CC-FB scan. This is shown in figure 7(b).

3. Imaging examples

Photoacoustic imaging was performed on solid phantoms embedded with tumour simulating inserts. The tissue component of the phantom was composed of poly(vinyl alcohol) (PVA) gel. The exact procedure for the making of the phantom has been detailed elsewhere (Kharine *et al* 2003, Manohar *et al* 2004). In short, the gel was prepared by submitting a 20% solution of PVA in water to four cycles of freezing and thawing; freezing to −20 °C for 12 h. Such a procedure imparts the gel with a reduced scattering coefficient (μ_s') of 0.5 mm^{-1} at 1064 nm. The absorption coefficient (μ_a) of the gel is 0.035 mm^{-1} at 1064 nm. The effective attenuation coefficient $\mu_e = [3\mu_a(\mu_a+\mu_s')]^{1/2}$ is calculated as 0.24 mm^{-1} which is close to values typically quoted for breast tissue in the NIR (Tromberg *et al* 2000, Spinelli *et al* 2004). Literature values of measured optical absorption contrast between tumours and healthy breast tissue are generally quoted as being between 1.25 and 3 (Tromberg *et al* 2000). We developed tumour inserts with a slightly higher absorption contrast of 4 with respect to the phantom, by dissolving PVA in dye solutions at the time of formation. Spheres of these gels were embedded in the phantom to simulate tumours (Manohar *et al* 2004).

The solid phantom was placed in the imaging tank (figure 2) filled with water. Light from the laser was allowed to impinge the phantom at regions where the inserts were expected. For a certain position of the light, an area of approximately 37 × 31 mm was covered, by reading out signals from a set of 120 elements; 12 in the *x* direction and 10 in the *y* direction.

Image reconstruction was performed using a delay-and-sum beamforming algorithm modified from Hoelen *et al* (2000). This applies a sliding window to each signal trace focused on each voxel into which the volume to be imaged is divided. Within the window, the peak–peak (maximum minus minimum) value of the signal is measured; these values for all elements are then summed, instead of the signal traces themselves. This can be expressed as,

$$S^V(t) = \frac{\sum_i w_i^V \left[S_i(t) h\left(t+\tau+\delta_i^V\right)\right]_{|\mathrm{mx}-\mathrm{mn}|}}{\sum_i w_i^V}, \tag{5}$$

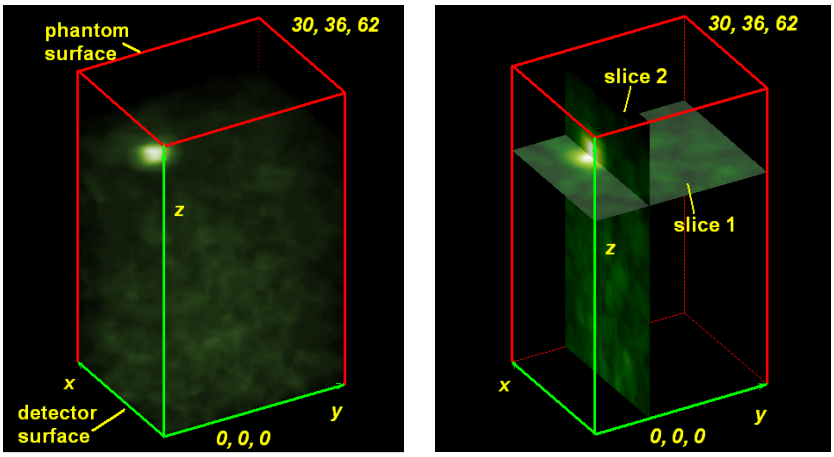

(a) (b)

Figure 9. Reconstructed phantom data in a volume of interest (VOI) visualized using (a) maximum intensity projection (MIP) in isometric view, and (b) orthogonal slices intersecting the reconstructed object. The VOI contained a 2 mm diameter sphere of absorption contrast 4, at a depth of 15 mm from the phantom surface.

where w_i^V is a weight factor which accounts for angular sensitivity, $S_i(t)$ is the signal, δ_i^V the delay applied, with i a specific detector element and V a specific voxel. The window function is defined by:

$$h(t+\tau) = \begin{cases} 1 & \text{for} \quad |t| \leqslant \tau/2, \\ 0 & \text{otherwise.} \end{cases} \tag{6}$$

Figure 9(a) is a maximum intensity projection (MIP) in isometric view of the 3D reconstructed data of a selected volume of interest (VOI) in the phantom. Figure 9(b) shows orthogonal slices passing through the reconstructed data for the same VOI. The VOI contained a 2 mm sized sphere with an absorption contrast of 4, at a depth of 15 mm from the surface. The dimensions of the VOI are $37 \times 31 \times 63$ mm. The voxel sizes chosen were $1 \times 1 \times 1$ mm in the x, y and z directions; the window size chosen as 2 mm. The light incident on the phantom was 50 mJ per pulse and signals were acquired after averaging 128 times.

4. Discussion

PAM is a first clinical prototype built around a flat, high-density ultrasound detector matrix. The detector is capable of imaging inhomogeneities of 2 mm diameter down to 32 mm depths with resolutions of 3.5 mm, in well-characterized phantoms. The imaging depths achieved use laser fluences at the surface conforming to laser safety standards for the specifications of light used. However, the resolution is specified for objects at the centre of the scanning area, a consequence of the planar geometry. This configuration does have the disadvantage of limited angular views when compared with the hemispherical TCT scanner (Kruger *et al* 2000) and the arc-array based LOIS (Oraevsky *et al* 1999); the former permitting a nearly complete 2π solid angle coverage and the latter upto 120°. The planar geometry does, however, facilitate convenient comparisons between images obtained with PAM and those from conventional x-ray mammography.

The resolution attainable using PAM is not as good as that quoted for the TCT scanner (Kruger *et al* 2002) which is between 1 and 2 mm, nor that quoted for LOIS which is 1 mm (Oraevsky *et al* 1999). Yet, we contend that this resolution is sufficient for the purposes of mammography. In addition, PAM provides 3D reconstructions using delay-and-sum beamforming algorithms. The LOIS is capable of 2D image slices, while the TCT imager does indeed provide truly 3D images.

In order to achieve deep (30+ mm) imaging with reasonable signal-to-noise ratios (SNR) using PAM, it is necessary to average the individual element signals upto 100 times. Additionally only one element can be accessed at a time. These two factors coupled with the 10 Hz laser pulse repetition rate ultimately set a ceiling on the number of elements that can be scanned in a practical period of time. This is the duration of time that a human subject can remain immobile with her breast in the scanner, without distress. This period is highly subjective but also depends on the patient–instrument interface. This has been the rationale behind the choice of the interface where the patient lies prone on a bed with the scanner beneath.

Based on healthy volunteer feedback, we have capped the measuring time to 45 min, which permits an area of 52×52 mm to be scanned with signal averaging of 100, and a pulse repetition rate of 10 Hz. Though this period of time is long for routine clinical examinations, it is admissible for the first human subject tests. The area of 52×52 mm allows resolutions between 3 and 3.5 mm to be achieved, assuming that the absorber lies in the centre of the scanning area. It remains then to ensure that the area of scanning with respect to the tumour size is adequate to obtain sufficient cancerous and healthy tissue in the examination region to establish figures of contrast.

The nature of the first phase of clinical studies is a retrospective evaluation of the technique, as embodied in PAM, for breast cancer detection. Subjects who have been diagnosed with breast cancer on the basis of clinical examination and diagnostic mammography, and have been scheduled for biopsy or surgery, will participate in this phase. Thus it will be possible to perform some pre-selection of subjects as possessing tumours which are likely to be manifested in a photoacoustic scan; tumours which are vascularized as indicated in MRI images. In addition, pre-selection based on the size constraints mentioned above will be possible. Positioning of the breast of the subject in the scanner to image the region-of-interest will be performed by the surgeon concerned with the case, directed by conventional images (x-ray, MRI, ultrasound) of the breast. A clinical protocol has been approved by a local medical ethical body, patient recruitment for the clinical study has commenced, and the first imaging experiments will begin shortly.

Technological improvements for this and subsequent phases are being explored. The long measuring time increases the chances of subject movement which can adversely affect the resolution and introduce artefacts. Reducing measurement time with the use of a higher repetition rate laser is being considered. A subject of ongoing work is hardware and software modifications required to implement a 10 parallel-output detector matrix.

Acknowledgments

We thank Rich Morris, Steve Morris and David Ergun of GE Medical Systems Lunar for useful discussions. We are grateful to Theo Pünt and Hans de Boer of the Mechanical and Physical Engineering Workshop for their ideas and support in the development of PAM. We thank Berry Westerhof of Schaeffler Nederland B.V. for discussions. Bob Visser of Clinical Instrumentation, Radiotherapy Department, Erasmus MC-Daniel, Rotterdam, is acknowledged for advice and help in bringing PAM to conform to electrical safety standards.

We thank Robert Molenaar for his involvement in some of the characterization studies. We acknowledge useful discussions with other members of the OPTIMAMM consortium, in particular with Heidrun Wabnitz, Dirk Grosenick, Jeremy Hebden, Robert van Veen, Dick Sterenborg and Thomas Moesta. The research was supported by the European Commission through the projects OPTIMAMM (contract no QLG1-CT-2000-00690; coordinator H H Rinneberg) and MEDPHOT (contract no QLG1-CT-2000-01464; coordinator R Steiner).

References

American Cancer Society 2004 Breast Cancer: Facts and Figures 2003–2004 *Technical Report*

Andreev V G, Karabutov A A and Oraevsky A A 2003 Detection of ultrawide-band ultrasound pulses in optoacoustic tomography *IEEE Trans. Ultrason. Ferroelectr. Freq. Control* **50** 1383–90

Folkman J 2000 Tumour angiogenesis *Cancer Medicine* ed J F Holland *et al* (Hamilton: B C Decker) pp 132–52, chapter 9

Grosenick D, Moesta K T, Wabnitz H, Mucke J, Stroszczynski C, Macdonald R, Schlag P M and Rinneberg H 2003 Time-domain optical mammography: initial clinical results on detection and characterization of breast tumors *Appl. Opt.* **42** 3170–86

Heffer E L and Fantini S 2002 Quantitative oximetry of breast tumors: a near-infrared method that identifies two optimal wavelengths for each tumor *Appl. Opt.* **41** 3827–39

Hoelen C G A and De Mul F F M 2000 Image reconstruction for photoacoustic scanning of tissue structures *Appl. Opt.* **39** 5872–83

Hoelen C G A, Dekker A and De Mul F F M 2001 Detection of photoacoustic transients originating from microstructures in optically diffuse media such as biological tissue *IEEE Trans. Ultrason. Ferroelectr. Freq. Control* **48** 37–47

Kharine A, Manohar S, Seeton R, Kolkman R G M, Bolt R A, Steenbergen W and de Mul F F M 2003 Poly(vinyl alcohol) gels for use as tissue phantoms in photoacoustic mammography *Phys. Med. Biol.* **48** 357–70

Kruger R A, Kiser W L Jr, Miller K D and Reynolds H E 2000 Thermoacoustic CT scanner for breast imaging: design considerations *Ultrasonic Imaging and Signal Processing (Proc. SPIE* vol 3982*)* ed K K Shung and M F Insana pp 354–9

Kruger R A, Kiser W L Jr, Romilly A P and Schmidt P 2001 Thermoacoustic CT of the breast: pilot study observations *Biomedical Optoacoustics II (Proc. SPIE* vol 4256*)* ed A A Oraevsky pp 1–5

Kruger R A, Stantz K and Kiser W L Jr 2002 Thermoacoustic CT of the breast *Physics of Biomedical Imaging (Proc. SPIE* vol 4682*)* ed L E Antonuk and M J Jaffe pp 521–5

Manohar S, Kharine A, Van Hespen J C G, Steenbergen W and Van Leeuwen T G 2004 Photoacoustic mammography laboratory prototype: studies on breast tissue phantoms *J. Biomed. Opt.* **9** 1172–81

Nass S J, Henderson I C and Lashof J C 2001 Mammography and beyond: developing technologies for the early detection of breast cancer *Report of the Institute of Medicine* (Washington, DC: National Academy Press)

Oraevsky A A, Andreev V G, Karabutov A A and Esenaliev R A 1999 Two-dimensional opto-acoustic tomography transducer array and image reconstruction algorithm *Laser-Tissue Interaction X: Photochemical, Photothermal and Photomechanical (Proc. SPIE* vol 3601*)* ed S L Jacques pp 256–67

Oraevsky A A, Andreev V G, Karabutov A A, Solomatin S V, Savateeva E V, Fleming R D, Gatalica Z and Singh H 2001 Laser optoacoustic imaging of breast cancer *in vivo Biomedical Optoacoustics II (Proc. SPIE* vol 4256*)* ed A A Oraevsky pp 81–94

Oraevsky A A and Karabutov A A 2003 *Optoacoustic tomography, Biomedical Photonics Handbook* ed T Vo-Dinh (Boca Raton: CRC Press) chapter 34, pp 1–31

Pogue B W, Poplack S P, McBride T O, Wells W A, Osterman K S, Osterberg U L and Paulsen K D 2001 Quantitative haemoglobin tomography with diffuse near-infrared spectroscopy: pilot results in the breast *Radiology* **218** 261–6

Sigrist M W and Kneubühl F K 1978 Laser-generated stress waves in liquids *J. Acoust. Soc. Am.* **64** 1652–63

Smith R A and Bacon D R 1990 A multiple-frequency hydrophone calibration technique *J. Acoust. Soc. Am.* **87** 2231–43

Spinelli L, Torricelli A, Pifferi A, Taroni P, Danesini G M and Cubeddu R 2004 Bulk optical properties and tissue components in the female breast from multiwavelength time-resolved optical mammography *J. Biomed. Opt.* **9** 1137–42

Suzuki K, Yamashita Y, Ohta K, Kaneko M, Yoshida M and Chance B 1996 Quantitative measurement of optical parameters in normal breasts using time-resolved spectroscopy: *in vivo* results of 30 Japanese women *J. Biomed. Opt.* **1** 330–4

Tromberg B J, Shah N, Lanning R, Cerussi A, Espinoza J, Pham T, Svaasand L and Butler J 2000 Non-invasive *in vivo* characterization of breast tumours using photon migration spectroscopy *Neoplasia* **2** 26–40

Van Staveren H J, Moes C J M, van Marle J, Prahl S A, Gemert Van and M J C 1991 Light scattering in Intralipid-10% in the wavelength range of 400-1100 nm *Appl. Opt.* **30** 4507–14

Van Veen R L P, Amelink A, Menke-Pluymers M, Van der Pol C and Sterenborg H J C M 2005 Optical biopsy of breast tissue using differential path-length spectroscopy *Phys. Med. Biol.* **50** 2573–81

Xu M and Wang L V 2003 Analytic explanation of spatial resolution related to bandwidth and detector aperture size in thermoacoustic or photoacoustic reconstruction *Phys. Rev.* E **67** 1–15